Review Article

Andreas Erdmann*, Dongbo Xu[a], Peter Evanschitzky, Vicky Philipsen, Vu Luong and Eric Hendrickx

Characterization and mitigation of 3D mask effects in extreme ultraviolet lithography

DOI 10.1515/aot-2017-0019
Received March 10, 2017; accepted April 6, 2017; previously published online May 10, 2017

Abstract: The reflection and diffraction of extreme ultraviolet (EUV) light from lithographic masks and the projection imaging of these masks by all-reflective systems introduce several significant imaging artifacts. The off-axis illumination of the mask causes asymmetric shadowing, a size bias between features with different orientations and telecentricity errors. The image contrast varies with the feature orientation and can easily drop far below intuitively expected values. The deformation of the wavefront or phase of the incident light by thick absorbers generates aberration-like effects, especially variations of the best-focus (BF) position vs. the pitch and size of the imaged patterns. Partial reflection of light from the top of the absorber generates a weak secondary image, which superposes with the main image. Based on a discussion of the root causes of these phenomena, we employ mask diffraction and imaging analysis for a quantitative analysis of these effects for standard EUV masks. Simulations for various non-standard types of mask stacks (e.g. etched multilayers, buried shifters, etc.) and for various non-standard absorber materials are used to explore the imaging capabilities of alternative masks for EUV lithography. Finally, an outlook at anamorphic systems for larger numerical apertures is given.

***Corresponding author: Andreas Erdmann,** Fraunhofer IISB, Schottkystr. 10, 91058 Erlangen, Germany,
e-mail: andreas.erdmann@iisb.fraunhofer.de
Dongbo Xu and Peter Evanschitzky: Fraunhofer IISB, Schottkystr. 10, 91058 Erlangen, Germany
[a]Present address: GenISys GmbH
Vicky Philipsen, Vu Luong and Eric Hendrickx: IMEC, Kapeldreef 75, B-3001 Leuven, Belgium

www.degruyter.com/aot

Keywords: computational lithography; EUV lithography; image modeling; mask technology; wave aberrations.

PACS: 42.25.-p; 42.30.-d; 81.16.Nd; 85.40.Hp.

Communicated by: Andreas Erdmann

1 Introduction

The highly parallel transfer of geometric patterns on photomasks into light-sensitive photoresists by optical projection imaging is one of the key technologies for the cost-effective manufacturing of integrated electronic circuits. The resolution limit of optical projection lithography for a wavelength λ and numerical aperture NA is given by the Rayleigh criterion $k_1\lambda/\mathrm{NA}$. The technology factor k_1 depends on the geometry of the illumination, on the mask technology, on the photoresist, and on several other process specific factors. It also expresses the fidelity of the image formation. For $k_1 > 0.6$, the created image provides an almost exact replica of the mask pattern. Smaller k_1 values result in increasingly severe deviations of the image from the original, such as rounding of edges, shortening of the ends of long features, or differences between the imaging characteristics of isolated and periodic objects. These so-called proximity effects are mainly caused by the diffraction limitation of the projection system. Optical proximity correction (OPC) applies corrections to the geometrical layout of the mask to pre-correct the image deformation. With a 1:1 duty ratio, $k_1 = 0.25$ provides the theoretical limit of single-exposure imaging of dense lines and spaces patterns. Nowadays, extensive optical proximity correction and multiple exposure/patterning techniques are employed to create sub-20-nm features with a wavelength of 193 nm and a numerical aperture of 1.35. The corresponding technology factor $k_1 < 0.15$ involves high costs for several mask sets and a large number of processing steps. The small wavelength of extreme ultraviolet (EUV) lithography at 13.5 nm promises a much easier imaging with relaxed k_1 values. For example, the

present pre-production tools with an NA of 0.33 enable the imaging of 20 nm features with a comfortable k_1 close to 0.5. Indeed, the first EUV printing experiments presented a superior image quality compared to deep ultraviolet (DUV) lithography [1].

A more detailed analysis of DUV and EUV imaging reveals that the interaction of light with the edges of mask features and multiple reflections of the diffracted light inside the mask stack introduce further deformations of the light in the near field and of the resulting projection images. These interactions become increasingly important, when the mask scale feature sizes are comparable and smaller than the wavelength of the used light or if the thickness of the absorber features is comparable or larger than the wavelength. This effect is not specific to EUV imaging. It was first observed in the analysis of the imaging of alternating phase shift masks (PSM) at a wavelength of 248 nm [2]. Light diffraction from the edges of the etched openings in alternating PSM causes an undesired intensity imbalancing between the etched and unetched openings of the mask.

The correct modeling of near-field interactions of the light with mask features requires an appropriate modeling approach. In the traditionally used Kirchhoff model, the transmitted/reflected light is directly obtained from the (flat) design of the mask. Considering a binary transmission mask as an example, the complete chromium-covered area has a transmission of 0, whereas the open area has a constant transmission of 1.0 (see left part of Figure 1). The phase of the transmitted light is constant. Rigorous electromagnetic computation of light diffraction from the mask, as shown in the right part of Figure 1, reveals important details on shape and phase of the transmitted light. For the used transverse electric (TE) polarization of the incident light, that is an electric field vector perpendicular to the drawing plane, a continuous transition of the intensity from the transparent open area to the dark chromium-covered area of the mask can be observed. The phase resembles a cylindrical wave with its origin at the center of the mask opening.

Projection of the transmitted near fields by a diffraction-limited optic reduces the differences between the images of the rigorously simulated masks and the Kirchhoff model, respectively. Nevertheless, some characteristic phenomena such as mask-induced polarization effects [3–5], mask-induced wave aberrations and best-focus (BF) shifts [6–8], and an impact on the obtained OPC models [9, 10] can be observed. These so-called 'three-dimensional (3D) mask effects' or 'mask topography effects' depend on the 3D geometrical shape of the mask and on the optical properties, specifically the extinction value k and the refractive index n, of the mask materials. The correct modeling of these effects requires a numerical solution of the Maxwell's equations by rigorously coupled wave analysis (RCWA or the related waveguide method), by finite-difference time-domain algorithms (FDTD) or by finite-element methods (FEM) – see, for example, Ref. [5] for a short introduction of these methods and further references.

All 3D mask effects, which are mentioned in the previous section, were observed for DUV lithography with transmissive masks. Despite the 4× reduction of state-of-the-art scanners, the feature sizes on the DUV masks are comparable or smaller than the used wavelength $\lambda = 193$ nm. The absorber thickness of the standard binary and attenuated PSM is small compared to λ. The optical

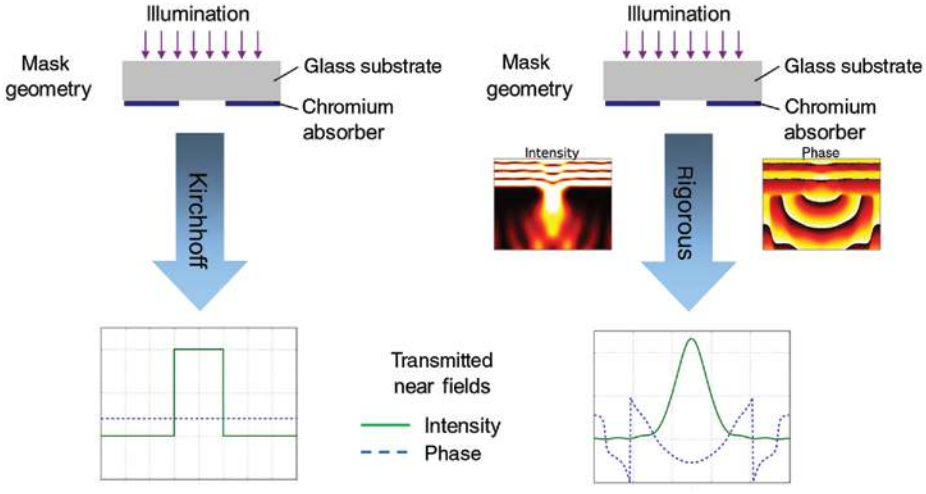

Figure 1: Mask models for the simulation of DUV lithographic imaging systems. Left: Kirchhoff approach, right: rigorous electromagnetic model. The schematic plots in the bottom exhibit the intensity and phase directly below the mask.

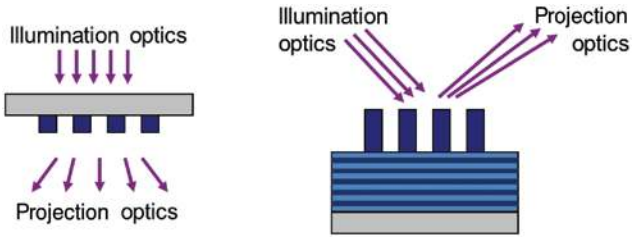

Figure 2: Schematic sketch of transmissive mask for DUV lithography (left) and reflective mask for EUV lithography (right). The multilayer of the EUV mask is only schematically shown. A real Mo/Si multilayer mask blank consists of about 40 bilayers of molybdenum and silicon.

constants n and k of the mask materials for the DUV light vary over a wide range. The high optical material contrast introduces a significant polarization dependency of the diffracted light. In contrast to the DUV masks, the mask for EUV are reflective (see Figure 2). A multilayer of Mo and Si reflects the incident light, whereas absorbers block the reflection and define the dark features on the mask. Considering the 4× reduction factor, the lateral size of the absorber features is larger than the wavelength of 13.5 nm. Also, the 60- to 80-nm-thick absorbers are thick compared to the exposure wavelength. The optical constants of all materials are very similar in the EUV spectral range with a refractive index n close to 1.0 and an extinction k between 0.0 and 0.08. Moreover, the reflective projection optics requires an asymmetric off-axis illumination of the mask.

The described similarities and differences between the DUV and EUV masks introduce several characteristic 3D mask effects in EUV lithography, which will be described in the following section. Section 3 introduces several mitigation strategies to reduce the negative impact of certain 3D mask effects on the image quality. A brief outlook on the expected 3D mask effects for anamorphic EUV systems with higher NA is given in Section 4.

2 3D mask effects in EUV imaging

The first investigations on the imaging performance of reflective EUV masks were already performed at the beginning of the nineties [11, 12]. Early simulation studies investigated feature orientation-dependent asymmetric shadowing effects as well as the influence of absorber and multilayer properties on the imaging performance [13–16]. This included also multilayer- and absorber-induced phase deformations and aberration-like imaging artifacts [14, 17, 18]. When EUV exposure tools became available, many of these simulation findings were experimentally validated [1, 19]. This section provides an overview of the most important 3D mask effects in EUV from today's perspective. Mask defects, especially multilayer defects, are not covered here because they have been addressed in other recent studies (see Refs. [20–23], for example).

2.1 Feature orientation and shadowing

The oblique illumination of the mask introduces an asymmetry of the diffraction pattern and of the resulting image. The chief ray angle (CRA) specifies the angle between the optical axis and the normal vector of the mask surface. The present EUV projection systems employ a CRA of 6°. Figure 3 illustrates the used naming conventions and coordinates. The mask surface defines the x and y planes. The CRA is tilted toward the y-axis. Vertical lines are oriented parallel to the y-axis, whereas horizontal lines are parallel with respect to x.

Figure 4 presents rigorously simulated near fields of vertical and horizontal lines. The arrows on the top illustrate the illumination direction. To highlight the impact of the CRA on the results, near fields for a standard CRA of 6° and for an increased CRA of 9° are shown in the upper and lower part of the figure, respectively. Larger values of CRA incease the asymmetric shadowing effects for horizontal lines. The asymmetric illumination of the horizontal lines causes a pronounced shadow on the left side of the absorber. The incident EUV light penetrates about 50 nm into the multilayer. Superposition of the incident and the reflected light generates a pronounced standing wave pattern in the absorber-free area of the mask. These standing waves have no impact on the image formation because incident and reflected light are spatially separated in the far field of the mask. The absorber blocks the multilayer

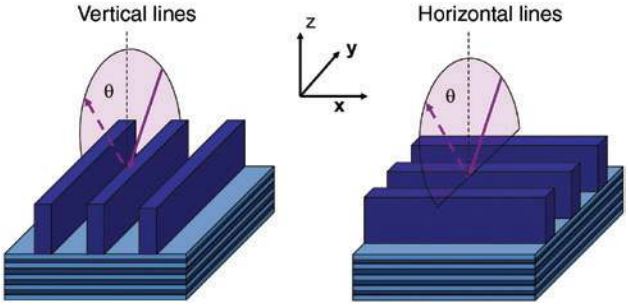

Figure 3: Mask geometries, coordinate system, and naming convention for vertical/horizontal lines. The arrows illustrate the direction of the incident and zero order-reflected light. For all simulations in this paper, the parameters of an experimentally characterized multilayer stack from Ref. [24] were used. The default absorber consists of an 80-nm-thick TaBN layer with n = 0.953 and k = 0.031.

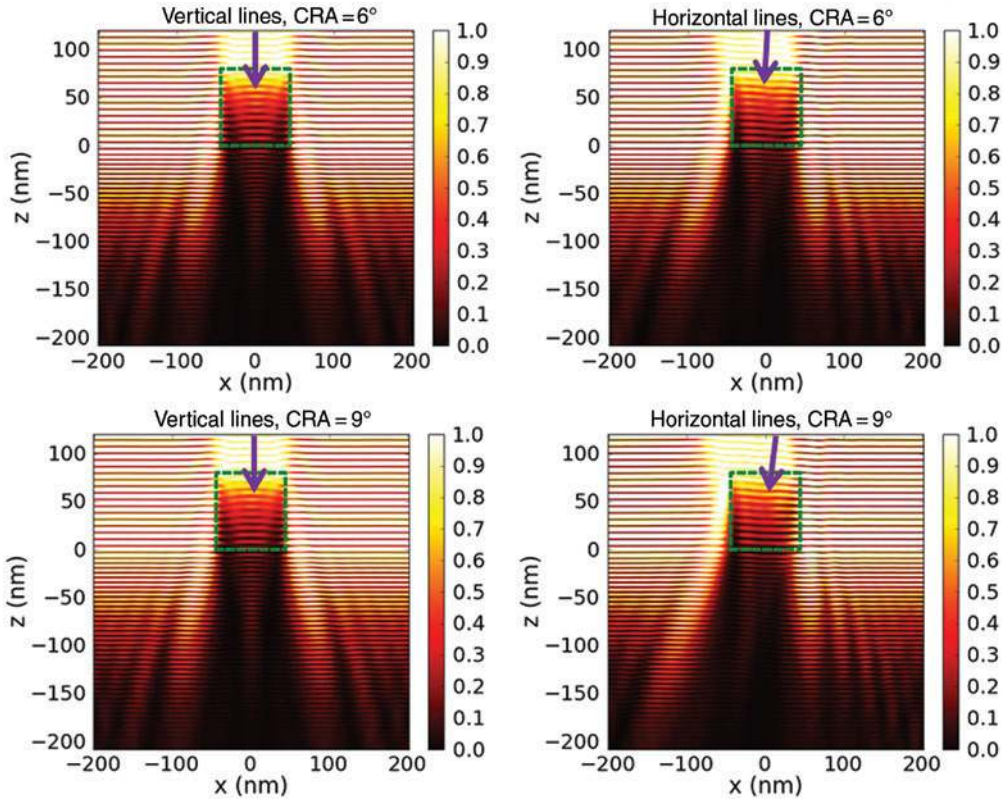

Figure 4: Simulated near fields for a top surface of the multilayer at z = 0 nm. The dashed lines indicate the position of the absorber. Incidend light: plane wave with a wavelength 13.5 nm and polarization perpendicular to the drawing plane, top: CRA of 6°, bottom: CRA of 9°. Absorber width and pitch 88 nm/400 nm on mask scale. All other parameters as given in Figure 3.

reflection at the position of the line. Only a small part of the light is reflected from the top surface of the absorber. The resulting effect will be discussed in Section 2.4.

The pronounced shadowing effect for horizontal lines can be also observed in the extracted cross sections of the reflected near fields directly above the absorber, which are shown on the left of Figure 5. The center and right part of this figure present the corresponding aerial image cross sections and lithographic process windows. A projection system with an NA of 0.33 does not resolve details of the symmetric/asymmetric oscillations of the near-field intensity around the line. However, the resulting image cross section exhibits a pronounced shift of the horizontal line to the left. Image shifts, which depend only on the feature orientation, can be easily compensated by a shift of the mask in the z-direction, the so-called mask focus position, and/or by simple rule-based OPC corrections of the mask layout [25]. The different shadowing of vertical and horizontal

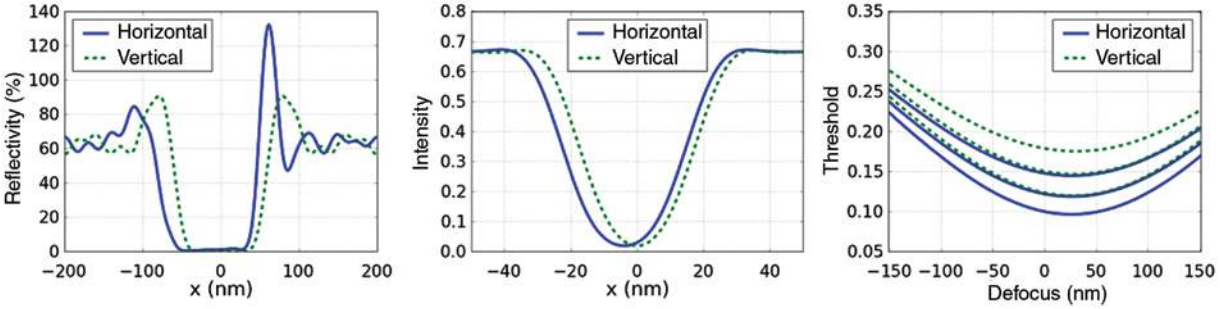

Figure 5: Reflected near fields directly above the absorber (left), aerial image cross sections (center), and lithographic process windows of vertical and horizontal lines. Imaging settings: NA = 0.33, 4× reduction, CRA = 6°, circular illumination with $\sigma = 0.7$, unpolarized light, target size: 22 nm ± 2.2 nm on wafer scale. All other parameters as given in Figure 4.

features causes a shift of the process windows along the threshold axis (see right of Figure 5). In general, horizontal features experience a more pronounced shadowing. A large part of this effect can be compensated by a simple orientation-dependent biasing of the mask layout or by a model-based OPC. The magnitude of the described orientation-dependent feature shifts and the required mask bias depend on the illumination, on the position of the feature in the exposure slit, and on the feature sizes and pitches.

Figure 6 demonstrates the dependency of the image asymmetry and feature shift of the 16-nm dense horizontal lines from the focus position. To highlight the impact of the CRA on the results, the simulation results for a standard CRA of 6° and for an increased CRA of 9° are shown on the upper and lower row of the figure, respectively. On the left and center column of the figure, aerial image intensities vs. focus position are plotted with two different ranges of the color contours. The contour range in the center column was chosen around the printing threshold. This emphasizes the variation of the feature position vs. the focus. The numerically extracted feature position vs. focus is given on the right column of the figure. Larger values of CRA incease the asymmetry of the images and the variation of the feature position vs. focus. The described effect presents a typical behavior of non-telecentric systems. The telecentricity error is obtained as the gradient of the feature position vs. the focus close to the center of the process window. It is expressed in nm placement error vs. micrometer defocus or millirad. The telecentricity error depends on the CRA, on absorber thickness, on the pitch, and on the shape of the illuminator.

2.2 Contrast fading

The spatially partial coherent illumination of the mask involves different illumination directions, which depend on the geometrical shape of the illuminator. Figure 7 exhibits a typical dipole illumination scenario for (horizontal) dense lines and space patterns. The left pole is tilted from the optical axis toward the normal vector of the mask surface. Therefore, the light hits the mask with almost vertical incidence and exhibits only a small asymmetry. The right dipole is tilted away from the normal vector of the mask surface. The light hits the mask at a large incidence angle of about 10° and generates a strongly asymmetric near field and diffraction pattern (see right part of Figure 7).

The differences between the near fields of the left and right dipole result in a very different non-telecentricity of the left and right pole. This can be seen in Figure 8, where the focus-dependent images, which are obtained with the individual poles, are plotted. The image of the right pole with the larger tilt angle exhibits a significantly larger non-telecentricity. Moreover, the increased shadowing for

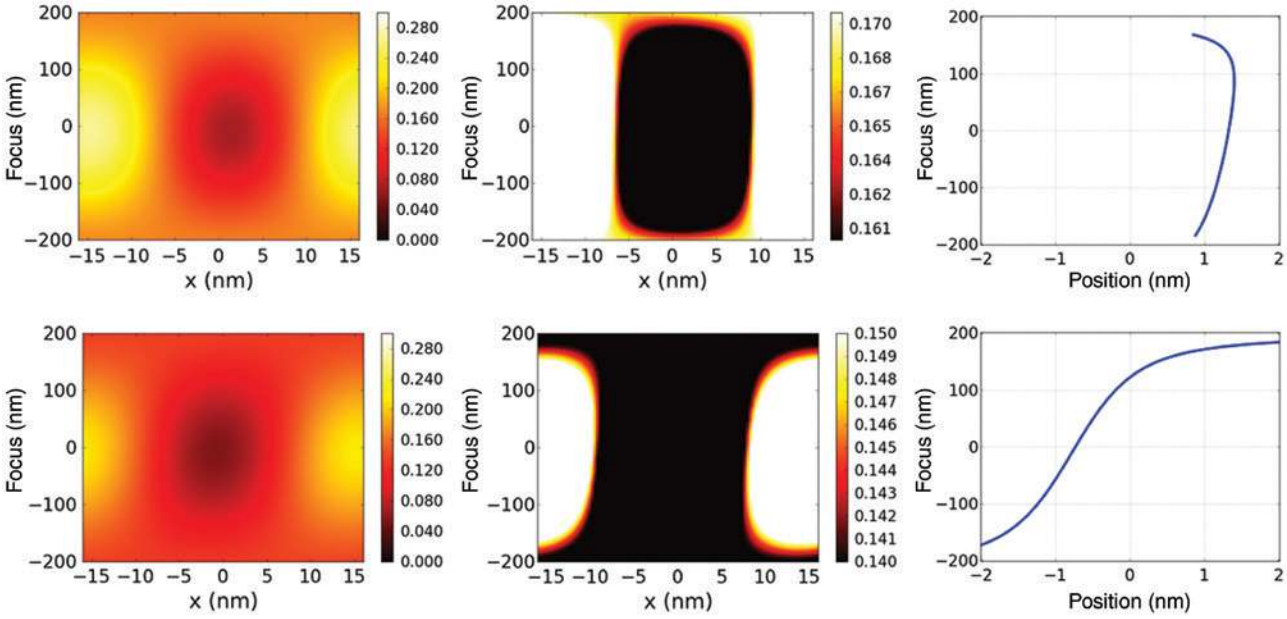

Figure 6: Demonstration of non-telecentricity of the EUV system for 16 nm lines with a pitch of 32 nm. Left and center column: plots of aerial image intensity vs. focus position for two different contour ranges, right column features position vs. focus. Imaging settings: NA = 0.33, 4× reduction, CRA = 6° (upper row) and CRA = 9° (lower row), annular illumination with $\sigma_{in/out} = 0.4/0.8$, unpolarized light. All other parameters as given in Figure 3.

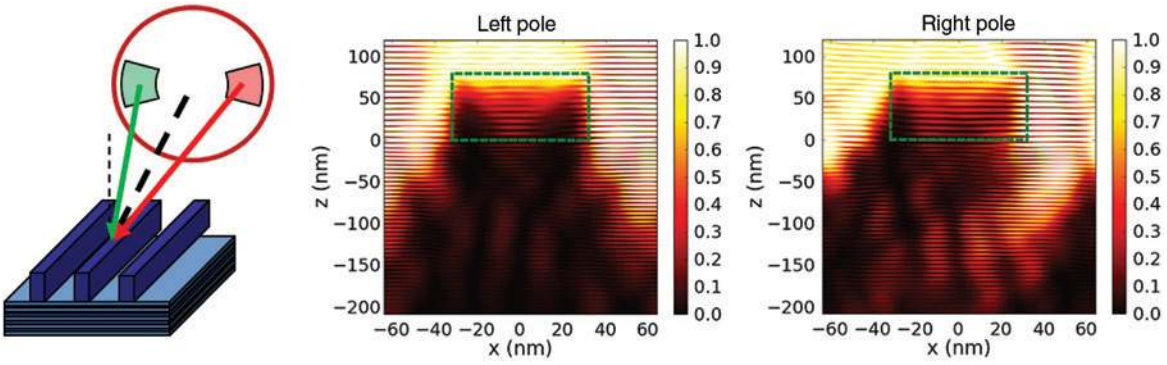

Figure 7: Dipole illumination scenario and simulated near fields for horizontal dense lines. Left: sketch of the mask geometry and illumination directions. The thin and thick dashed lines show the direction of the mask surface normal vector and of the chief ray angle, respectively. The circle and segments indicate a numerical aperture of 0.33 and the positions of the left and right pole in the illuminator. Center and right: simulated near fields for illumination from the center of the left/right pole. Absorber width: 64 nm on mask scale, pitch: 128 nm on mask scale. All other parameters as given in Figure 3.

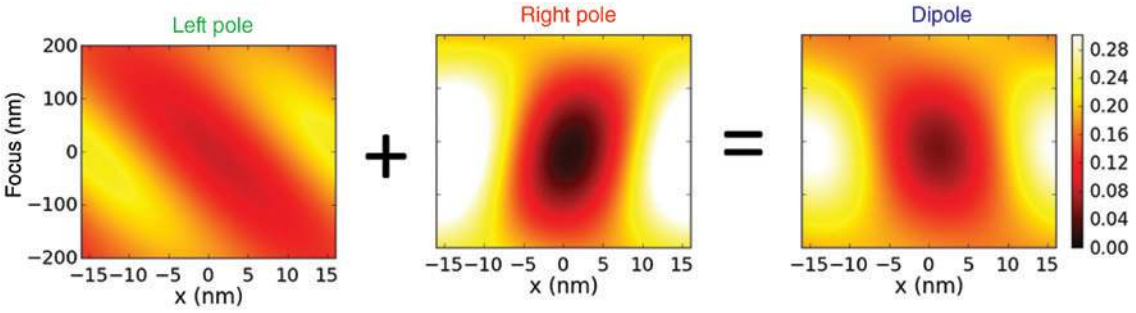

Figure 8: Plots of aerial image intensity vs. focus position for left pole, right pole, and complete dipole. Imaging settings: CRA = 6°, dipole illumination with $\sigma_{in/out} = 0.4/0.8$ and 30° opening angle, unpolarized light. All other parameters as given in Figure 7.

the right poles increases the imbalance of the intensity of the imaging-relevant diffraction orders and decreases the contrast. The image for the complete dipole is obtained by the incoherent superposition of the images for the individual poles. The different positions of the intensity minima of the left/right pole and the different non-telecentricity cause a further fading of the contrast. See also Refs. [26] and [27] for a detailed discussion of this effect.

2.3 Phase deformation and best-focus shifts

The near-field interaction of the incident light with the thick absorber and the multilayer impacts not only the intensity but also the phase of the diffracted and reflected light. This is demonstrated in Figure 9, where the near-field intensity and phase of semidense lines and semidense spaces are shown. For the benefit of a clearer visualization of the relevant effects, the intensity and phase distributions were computed without the reflective multilayer. The absorber consists of an 80-nm-thick TaBN layer with the refractive index n = 0.953 and the extinction coefficient $k = 0.031$. The phase front propagates faster inside the absorber with a refractive index, which is smaller than 1.0. Because the light is absorbed in this part of the mask, the phase is not important for the resulting image. However, the phase deformation also extends into regions outside of the absorber, where intensities are significant for the image formation.

The deformation of the phase in the near-field transfers into a phase deformation of the far field of the diffracted light at the entrance pupil of the projection system. Therefore, the mask-induced phase effects generate imaging effects, which are very similar to phase deformations, which are caused by wave aberrations of the projection systems. One of these effects, the shift of the BF position between dense and isolated features, is presented in Figure 10. Here and in the remaining part of this paper, the BF is defined by the focus position with the largest normalized image log slope (NILS). More detailed discussions on the pitch dependency of BF shifts, tilts of process windows, and several related effects can be found, for example, in Refs. [28] and [29].

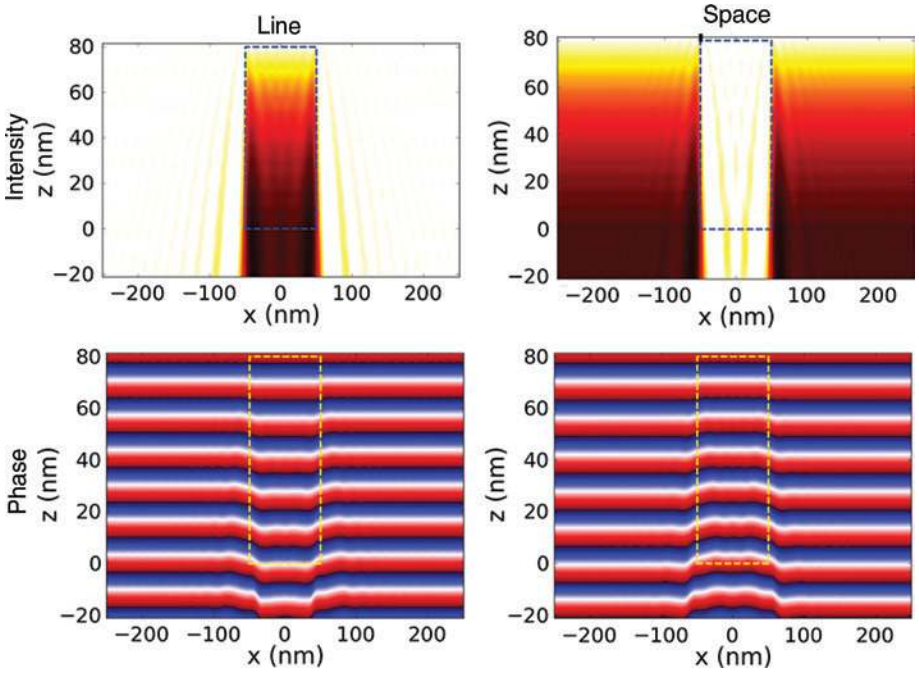

Figure 9: Near-field simulation for an EUV mask without reflective multilayer: TaBN absorber with 88-nm mask scale feature size and 220-nm mask scale pitch. Top: near-field intensities, bottom: near-field phase, left: line feature, right: space feature. Feature orientation: vertical, CRA 6°, polarized light with a wavelength $\lambda = 13.5$ nm and an electric field vector parallel to the lines, dashed line – outline of absorber.

2.4 Double images and absorber thickness swings

Another 3D mask effect can be attributed to the reflective character of the mask. The dominating part of the reflected light originates from the multilayer, which is designed to provide a high reflectivity over a sufficiently large range of incidence angles. However, there is also some reflected light from the top of the absorber. This is illustrated in Figure 11. The lower row of this figure presents the near-field intensity in the vicinity of the absorber, the reflected intensity at the top of the absorber, the resulting images, and process windows of an EUV absorber without multilayer. Although the intensity of these secondary images of the reflected light from the top of the absorber is small compared to the image intensity of the total reflected light, it cannot be neglected.

These secondary images are contrast reversed with respect to the total image. Secondary images of vertical and horizontal features are almost identical. They do not exhibit significant asymmetries or feature shifts. However, their BF deviates considerably from the BF of the total image. This total image is obtained as an interference of the top absorber-reflected image and of the

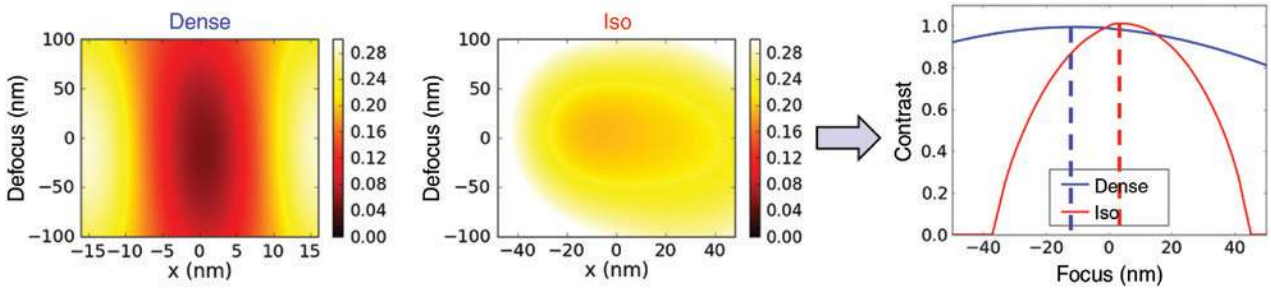

Figure 10: Simulation of mask-induced BF shifts: left and center: plots of aerial image intensity vs. focus position for dense and isolated horizontal lines; right: normalized local contrast (NILS) of dense and isolated features vs. focus. Mask scale feature size: 88 nm mask scale, dipole illumination with $\sigma_{in/out} = 0.4/0.8$, and 30° opening angle. All other parameters as given in Figure 8.

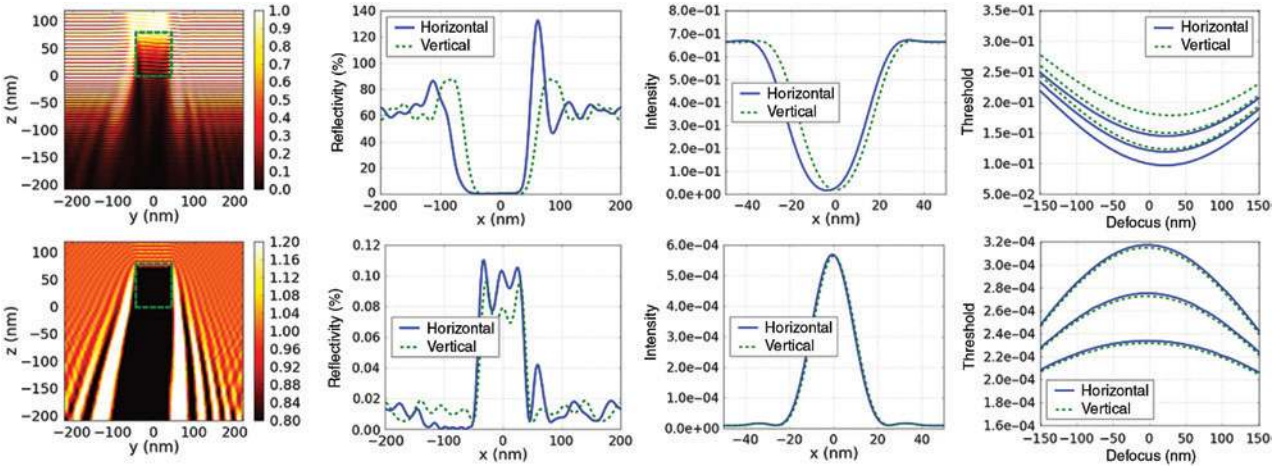

Figure 11: Simulated near fields (for horizontal lines only) in the vicinity of the absorber pattern, reflected light at the top of the absorber, aerial images, and lithographic process windows (from left to right) for a standard EUV mask with reflective multilayer (top) and without multilayer (bottom). Absorber width: 88 nm on mask scale; pitch: 440 nm on mask scale. All other parameters as given in Figure 3.

multilayer-reflected image. The result of this interference depends on the thickness of the absorber layer. The interference effect and the variation of the phase shift between the top absorber-reflected and the multilayer-reflected light with the absorber thickness generate a swing behavior of the total amount of the total reflected light. In addition to this well-known reflectivity swing, such swing behavior is also observed for other imaging characteristics like NILS and BF (see Figure 12).

3 Mitigation strategies

The examples from the previous section have demonstrated the mostly unfavorable impact of 3D mask effects on the lithographic process performance. A significant component of the orientation-dependent feature placement and size effects can be compensated by a proper choice of the mask focus and by an OPC of the mask pattern. However, the dependency of the required corrections on the position in the scanner slit, on feature size/pitch, and on the illumination geometry make the OPC flow increasingly difficult. Other effects like contrast fading and pitch-dependent shifts of the BF position cannot be compensated by OPC. Therefore, other solutions to mitigate the 3D mask effects are indispensable.

Several authors including ourselves have investigated the option to compensate the mask-induced phase effects and BF shifts in the DUV systems by dedicated wave aberrations of the projection lens [30–32]. However, the introduced wave aberrations of the projection lens can potentially have a negative impact on other features in the layout. In comparison to the DUV systems, which offer extensive possibilities for wavefront manipulation [32], the present EUV systems provide only limited possibilities for the manipulation of the wavefront. In the following, an

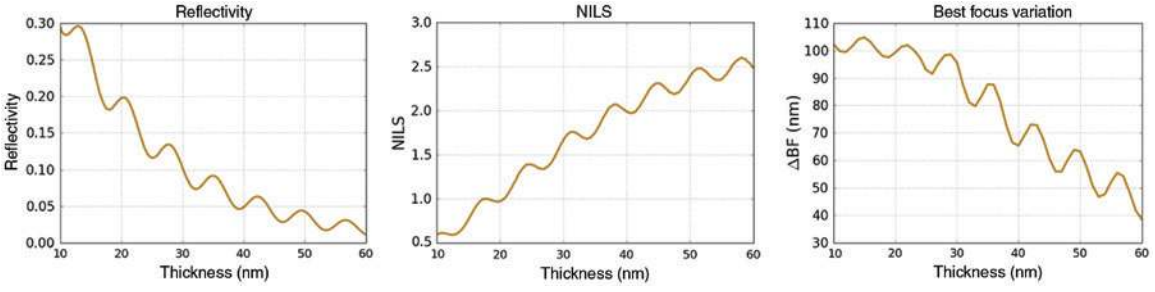

Figure 12: Total reflectivity of the unpatterned absorber (left), NILS (center) and BF position (right) vs. thickness of a TaBN absorber. Mask scale feature size: 88-nm mask scale, CQuad illumination with $\sigma_{in/out} = 0.4/0.8$, and 30° opening angle. All other parameters as given in Figure 3.

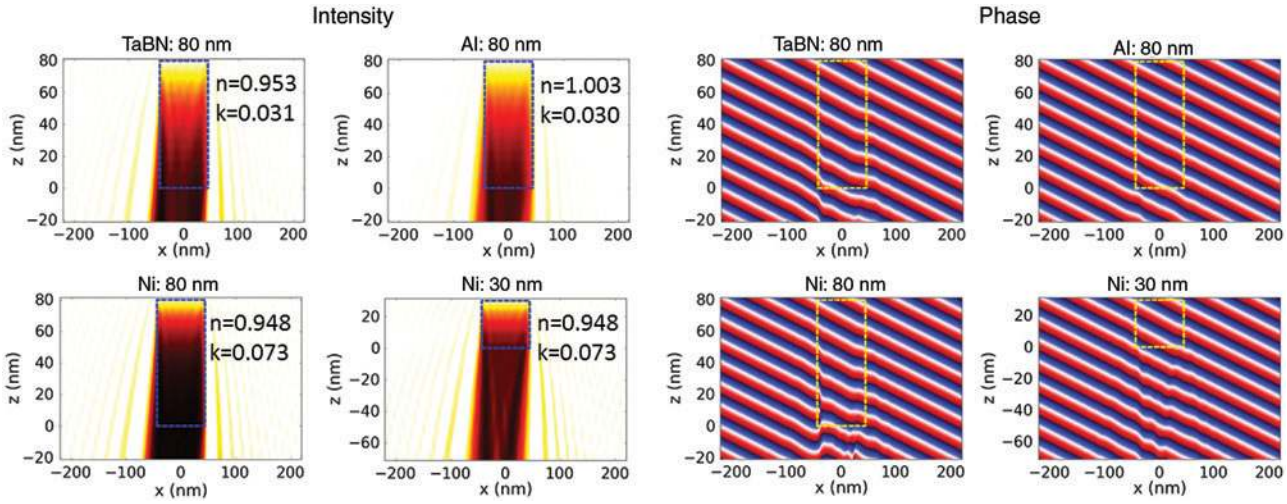

Figure 13: Near-field simulation for different absorber materials. Top: 80-nm-thick TaBN and 80-nm-thick Al absorber; bottom: 80-nm- and 30-nm-thick Ni absorber. Left: near-field intensities, right: near-field phase. Feature orientation: horizontal. The n and k values of the materials are given in the text on the left of the figures. All other parameters as given in Figure 9.

overview on mitigation strategies by manipulations of the mask and of the illumination is given.

3.1 Absorber material and thickness

The most straightforward, but also technically challenging, solution is to replace the state-of-the-art tantalum-based absorber by materials with a larger extinction coefficient, which enable thinner absorber layers. Another possible direction for improvement could be a material with a refractive index closer to 1.0. Such material would reduce the phase deformation by the absorber. Figure 13 compares the near-field simulations for two candidate absorber materials to that one of the standard TaBN absorber material. Similar to Section 2.3, the intensity and phase distributions were computed without the reflective multilayer. This enables a more straightforward interpretation of the results.

The phase deformation of the nickel absorber on the bottom row of Figure 13 is comparable to that one of TaBN. This is not unexpected because the refractive index of these materials is also very similar. However, the large extinction of the Ni results in a fast drop of the intensity in the upper part of the absorber. The near-field simulations for the 30-nm thick on the bottom row of the figure indicate that the absorber thickness can be reduced without a significant loss of contrast. The Al absorber on the top row of Figure 13 has a refractive index very close to 1.0 and exhibits an almost negligible phase deformation. On the downside, there is a significant contrast loss compared to the other stacks, especially in the area below the absorber. Such contrast loss makes it at least questionable, whether an 80-nm-thick aluminum absorber provides sufficient image contrast.

Quantitative comparisons of different absorber materials can be performed by mask diffraction analysis or by full image analysis. Mask diffraction analysis does not require image simulations [5]. It can be used for a quick pre-screening of candidate materials and thickness ranges. An example is given in Figure 14, where diffraction simulations for lines and space patterns with different pitches p and orientations are used to determine a characteristic phase deformation for a given material and thickness. Except for the zeroth diffraction orders, the phase values of all other orders lie on an imaginary phase front. The phase offset of the zeroth order and the fit coefficients of the imaginary phase front with Zernike polynomials provide characteristic numbers, which contain the key information on the mask-induced phase deformation and aberration-like effects, which can be expected for a specific absorber material and thickness.

The data on the right of Figure 14 compare the simulated phase offsets and Zernike tilt coefficients of Ni, TaBN, and Al vs. the absorber thickness. As expected from Figure 13, Al exhibits the lowest phase deformation. The Ni absorber has a lower phase offset than TaBN. The Z2 coefficients of TaBN and Ni are similar.

The mask diffraction analysis is complemented with a more comprehensive image analysis for line and space pattern as shown in Figure 15. The data on the upper left of the figure present computed BF positions vs. thickness (horizontal axis) and pitch (vertical axis). The BF varies between negative values for dense patterns (small pitches) and positive values of the BF position for pitches around

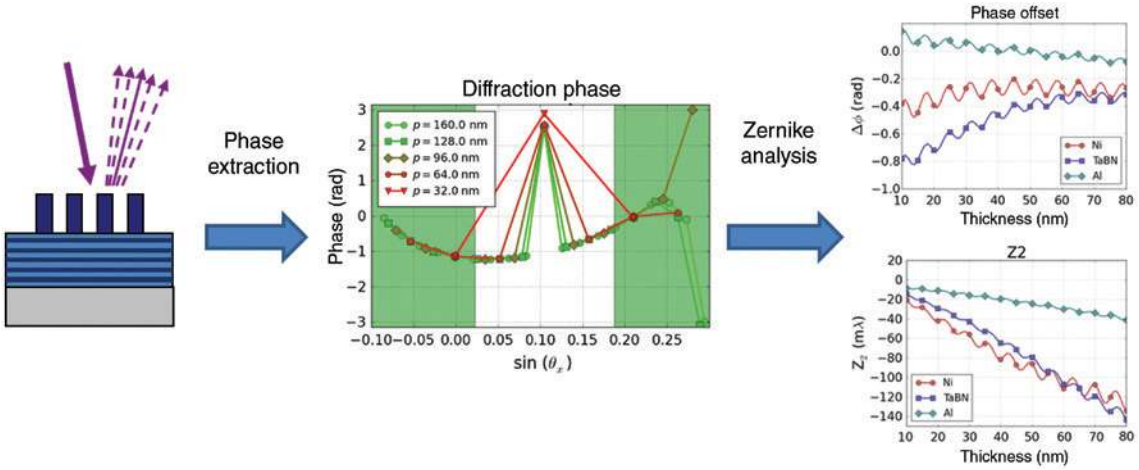

Figure 14: Diffraction and Zernike analysis of mask absorber materials. Left: schematic setup – a line and space pattern is illuminated by a plane wave. Center: the phase of propagating diffraction orders with respect to the phase of the incident light is measured/computed for different pitches *p*. The bright area at the center of the plots indicates the range of propagation angles inside the numerical aperture. Right: extracted Zernike fit coefficients for different absorber materials and thickness values. Details about this method are given in Refs. [28] and [29].

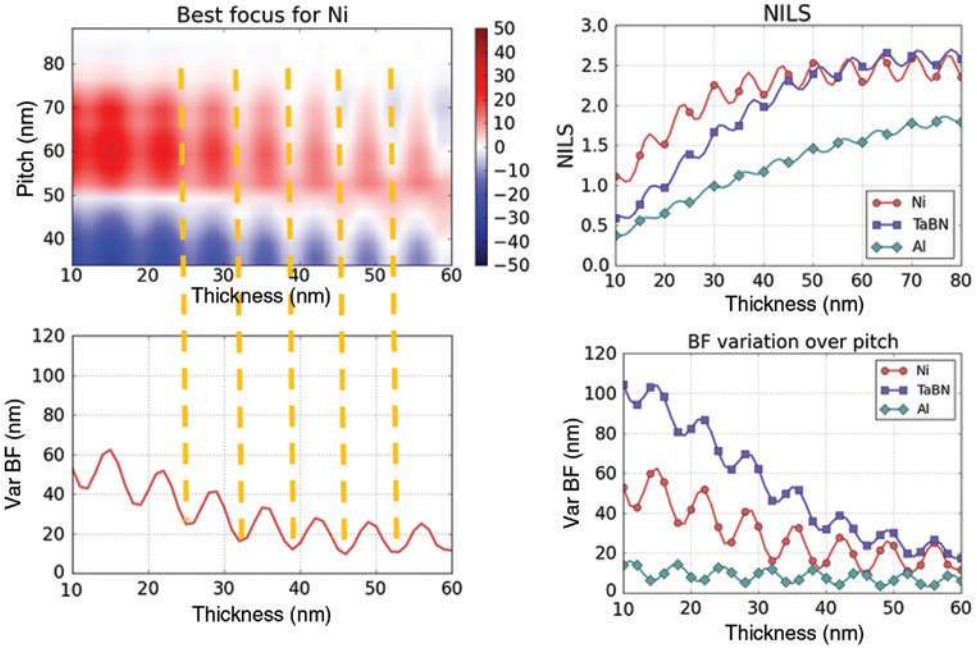

Figure 15: Imaging analysis of mask absorber materials. Left: procedure for the evaluation of the BF variation. Right: NILS and BF variation of dense features vs. absorber thickness for Al, Ni, and TaBN absorbers. All simulation settings as specified in Figure 12.

65 nm for all considered absorber thickness values. The magnitude of the BF variation decreases with the absorber thickness. This is also seen on the lower left of the figure, where the range of the BF variation over all pitches is plotted vs. the absorber thickness. The swing behavior of this curve is attributed to the 'double image' phenomenon, which was described in Section 2.4.

Similar curves can be computed for other absorber materials as well (see lower right part of Figure 15). Again, Al exhibits the best performance. The Ni absorber behaves significantly better than the standard TaBN absorber material. The data on the upper right of Figure 15 compare simulated NILS values of dense features of the three considered absorber materials vs. thickness. According to these data, a 30-nm-thick Ni absorber can offer sufficient contrast. Aluminum cannot provide sufficient contrast, even for a thickness of 100 nm. This excludes aluminum from the list of candidates for alternative single-layer

absorbers. More details on the comparison of these and other absorber materials including experimental investigations are published in Ref. [33].

3.2 Alternative mask stacks

Alternative mask stacks such as etched or locally shifted multilayers can provide additional degrees of freedom to mitigate 3D mask effects. Various forms of etched multilayer configurations were proposed and investigated with the goal to realize phase shift masks for EUV lithography [34–37]. Aside from the technical challenges to fabricate these masks, the design and the comparison of their lithographic performance to standard mask stacks is far from trivial. Multiple criteria such as image contrast, total amount of reflected light that contributes to the image formation, BF variation, and telecentricity error, have to be considered in the performance evaluation of these masks.

Figure 16 presents selected results of a multi-objective optimization study of alternative mask stacks for EUV [38]. Three different types of mask stacks were investigated. The standard binary mask (BIM) on the left consists of two absorber layers on the top of a Mo/Si multilayer stack, which is separated into two different bilayers with variable total thickness and thickness ratio. The etched PSM stack at the center of the figure represents a standard etched multilayer with an etch stop layer and an additional absorber layer inside the etched part of the multilayer. The nominally dark features of the embedded shifter PSM stack on the right are defined by a thin shifter layer, which separates the lower and upper part of the multilayer. The purpose of this shifter layer is to generate a destructive interference of light, which is reflected from the lower and upper part of the multilayer, respectively. Considering variable thickness values of the absorber layers, shifter layer and multilayers, as well as numbers of etched/shifted layers and feature size biasing, each type of stack has about 10 design variables. A multi-objective genetic algorithm was applied to optimize these stacks for four (scalar) objectives: maximum local contrast (NILS), maximum total reflectivity or threshold to size, minimum telecentricity error, and minimum BF variation over pitch.

The data in Figure 16 present a 2D cut of a 4D Pareto front, which identifies appropriate compromise solutions with respect to all four considered objectives. The horizontal axis specifies the threshold to size, which should be as large as possible to achieve a high throughput of the lithographic system. The vertical axis gives the NILS or local contrast, which should be as large as possible to enable a large dose latitude. Consequently, the most appropriate solutions can be found in the direction of the upper right of the graphs. The two slightly larger red circles are reference values of the presently used TaBN mask stacks with an absorber thickness of 56 nm and 70 nm, respectively.

The achievable solutions for the standard mask stack with variable absorber and multilayer thickness are not much better than the reference values. In other words, the thickness values of the presently used stacks represent already a reasonable compromise between high threshold/throughput, high contrast, and other lithographic performance metrics. The etched PSM at the center of the figure can perform slightly better. The best performance can be achieved with the embedded shifter PSM. A more detailed analysis and comparison of the different masks is presented in Ref. [38]. Selected experimental investigations on some of these alternative masks are reported in Ref. [39].

3.3 Sub-resolution assist features

Sub-resolution assist features (SRAFs) are established in DUV lithography to increase the depth of focus (DoF) of

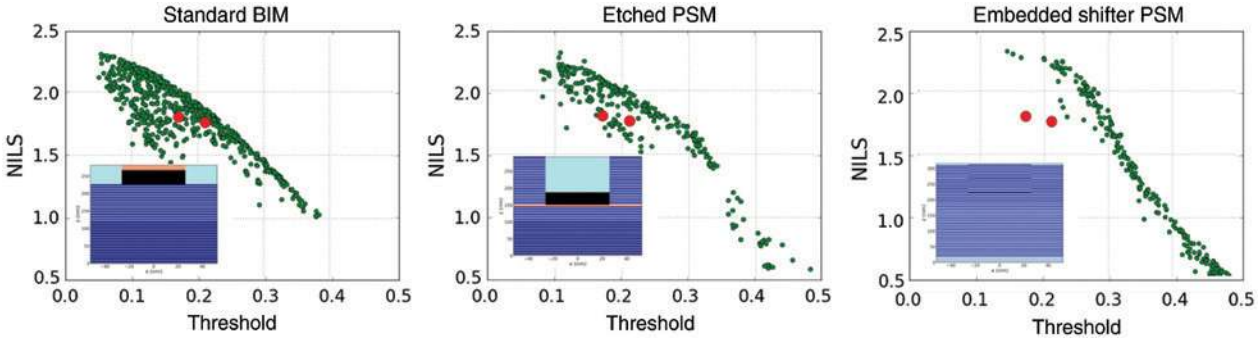

Figure 16: Typical Pareto fronts for multi-objective optimization with different mask types, NILS fitness vs. threshold fitness. The figure insets show the basic geometry of the investigated masks. See Ref. [38] for details.

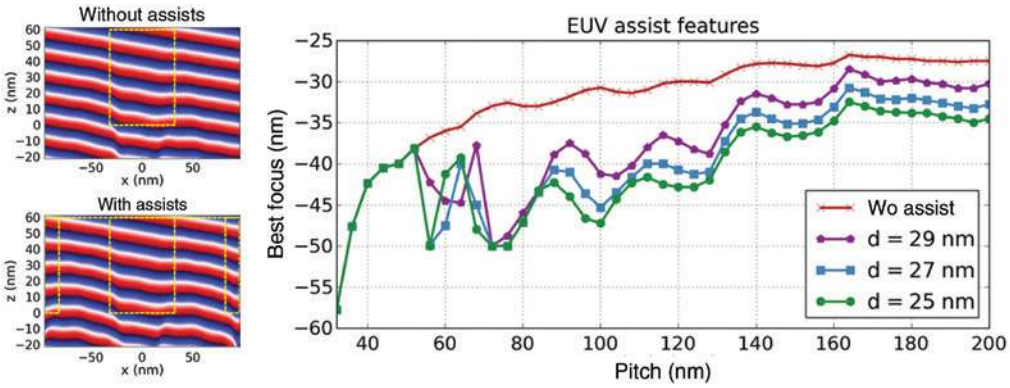

Figure 17: Simulated impact of assist features on the dependency of the BF of 16-nm lines from pitch. Left: simulated phase of the near field without and with assist features. Dashed lines indicate the outline of the line and assist features. Right: BF vs. pitch for different assist, d specifies the distance of the assist center from the center of the main feature on wafer scale. Imaging settings: CRA = 6°, dipole illumination with $\sigma_{in/out} = 0.7/0.9$, and 35° opening angle, unpolarized light. Mask stack as given in Figure 3.

semi-dense and isolated features. It has been shown that they can be also used to reduce the differences between the BF position of dense and isolated features [40–42]. The impact of assist features on the phase of the near field and on the BF vs. pitch is demonstrated in Figure 17. Wider assist features reduce the difference between the diffraction spectra and the BF positions of dense and isolated features. Asymmetric assists provide an additional degree of freedom. Appropriate extensions of OPC algorithms for the placement and sizing of assist features are required, to incorporate the impact of the assist features on the BF performance. Detailed investigations on the impact of SRAFs on the symmetry of Bossung curves and process windows were recently published by Wang et al. [43].

3.4 Source optimization

The mask-induced deformation of the wavefront depends strongly on the illumination direction. This dependency can be exploited in an optimization of the source shape to mitigate the 3D mask effects [44, 45]. Figure 18 presents a demonstration for a horizontal double slit configuration, which is highly sensitive to 3D mask effects. The plot of the focus dependency of the aerial image for a standard dipole illumination on the upper left of the figure exhibits a pronounced asymmetry. The BF positions of the slits differ by almost 50 nm. This pronounced focus shift can be almost completely compensated by appropriate optimization of the source geometry. The focus-dependent aerial images and extracted feature sizes of the optimized asymmetric source are shown on the right of the figure. Special care has to be taken during the source optimization to keep the high contrast and to avoid the introduction of extraordinary aberration sensitivities.

4 Larger NA systems for EUV

The increase in the numerical aperture means larger wafer-side angles. For the same de-magnification of the system, this involves also larger angles on the mask side. For NA > 0.5 and when maintaining 4× de-magnification, the chief ray angle has to be increased from 6° to 9°. The combination of 3D mask effects and large ranges of incidence angles results in non-manageable contrast loss and of feature orientation dependencies [46]. Increasing the de-magnification from 4× to 8× would help to stay with the 6° CRA, but reduces the throughput of high NA scanners by an unacceptable factor. Anamorphic systems with an 8× de-magnification in the tilt direction of the chief ray, which is identical with the scan direction, and a 4× de-magnification in the orthogonal direction, have been identified as an appropriate method to resolve the described conflict between image quality and throughput [47, 48].

Figure 19 presents the computed reflectivity of the mask multilayer stack of the three alternative systems within the numerical aperture. The standard Mo/Si bilayer mask blank cannot support the large range of mask side incidence angles and the required CRA of 9° of the 4×/4× system. The significant drop of the multilayer reflectivity at angles, which are close to the right edge of the projector pupil, generates unacceptable contrast loss, especially for dense horizontal features. Both the 8×/8× and the anamorphic 8×/4× exhibit an almost uniform reflectivity of the mask multilayer substrate within the relevant range of incidence angles.

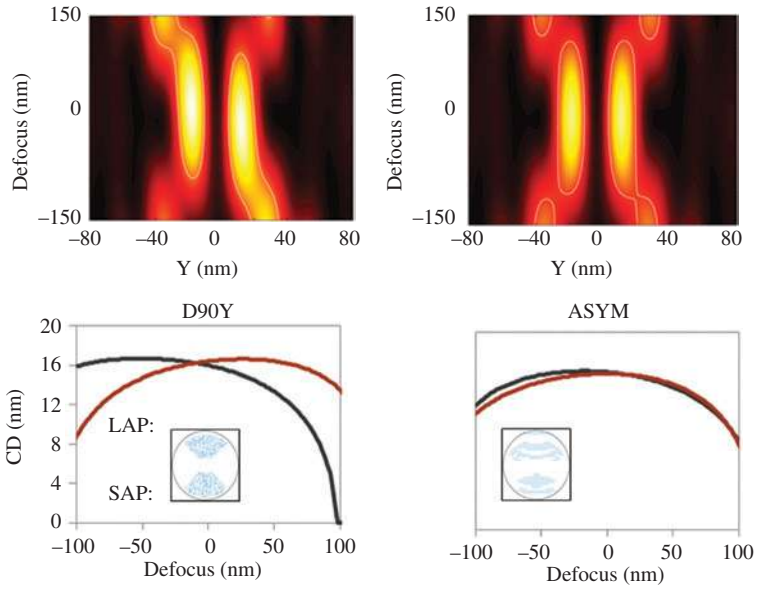

Figure 18: Simulation of the imaging of horizontal double slits with standard dipole (left) and optimized asymmetric illumination (right). Top: plots of aerial image intensity vs. focus, bottom: extracted printed feature size or critical dimension (CD) of upper (large Y) and lower slit (small Y) vs. focus; the illumination shapes are shown in the corresponding figure insets. LAP, large-angle pole; SAP, small-angle pole. Figure adapted from Ref. [44] with permission of the authors.

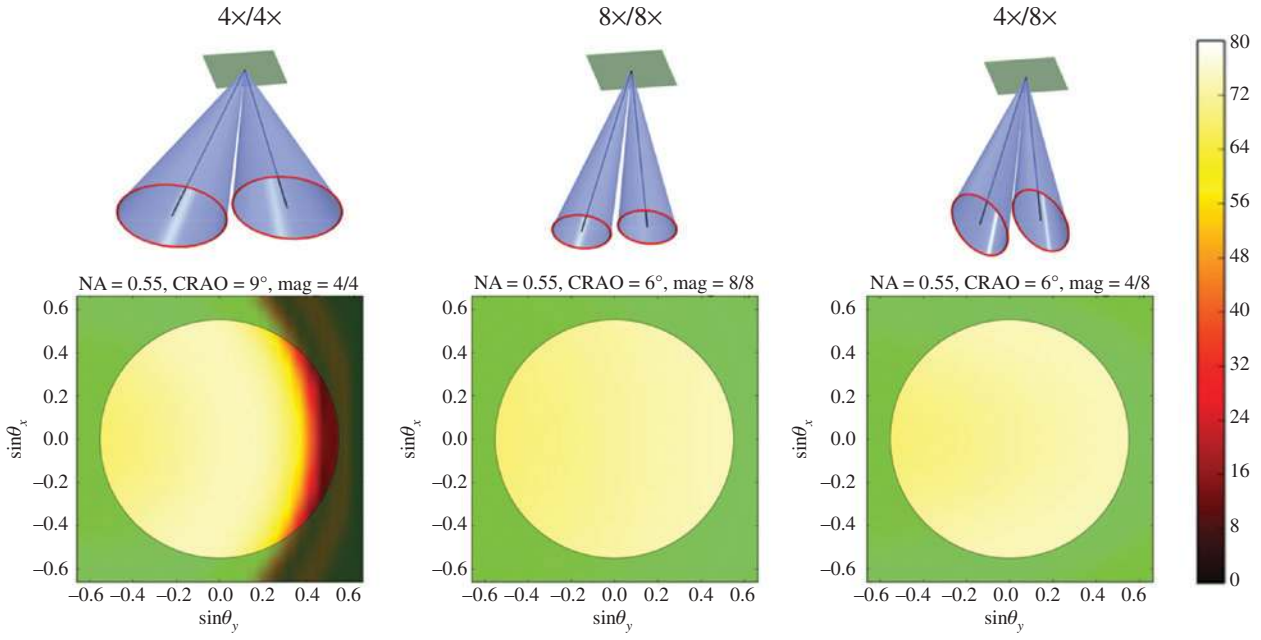

Figure 19: Simulated reflectivity of the standard Mo/Si multilayer mask blank vs. the relevant range of incidence angles of the 4×/4× system (left), of the 8×/8× system (center), and of the anamorphic 4×/8× system. The angular ranges in x- and y-directions are specified on wafer scale. The circles indicate the edges of the numerical aperture NA = 0.5. The sketches of the mask side incidence angles on top were adapted from Ref. [49]. The multilayer parameters were taken from Ref. [24].

Figure 20 compares the simulated NILS values of 8-nm vertical and horizontal lines with a pitch of 16 nm for the three considered systems. Note the significant drop of the NILS value of the 4×/4× system for the horizontal lines. Conversely, the local contrast of the 8×/8× and the anamorphic 8×/4× is close to the contrast of the vertical lines.

The last example in Figure 21 presents simulated elbow structures for the three considered systems. As expected, the 3D mask effects introduce a significant

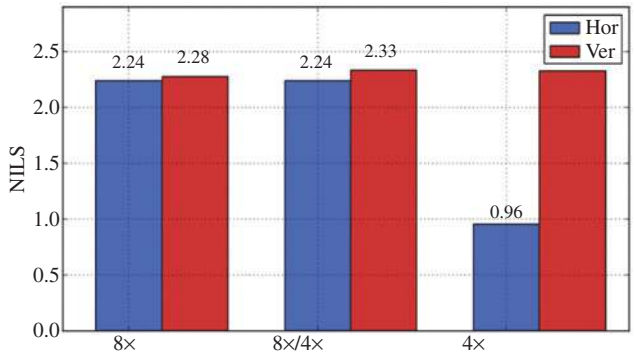

Figure 20: Simulated NILS of 8-nm lines with a pitch of 16 nm for NA = 0.52 systems with a central obscuration, unpolarized leaf-shaped illumination and various de-magnifications. CRA: 9° for the 4×/4× system and 6° for the other systems. Mask stack as given in Figure 3.

loss of intensity and contrast for the horizontal arms of the elbow. Both the pure 8× and the anamorphic system can completely recover these losses. Such behavior was recently confirmed by experiments on the SHARP microscope [50].

5 Conclusions and outlook

The described phenomena and examples have demonstrated that 3D mask effects need to be considered in the design of EUV systems and in OPC algorithms for EUV lithography. The combination of asymmetric illumination and 3D masks introduces an orientation dependency of the size and position of the printed features and significant contrast losses. The observed phase deformation is governed by the thickness and refractive index of the absorber material. It results in feature-dependent BF shifts and asymmetric process windows. The interference of a primary image, which is obtained by reflected light from the multilayer, and a significantly weaker secondary image, which results from reflected light from the top of the absorber, generates sinusoidal variations of all important image quality measures vs. the absorber thickness.

Although the sensitivity of patterns and illumination settings to 3D mask effect varies for industry-relevant patterns [33], the application of mitigation strategies to reduce the unfavorable impact of 3D mask effects is indispensable. Optimization of asymmetric source shapes and assist features can provide near-term solutions, but require appropriate OPC and source-mask-optimization (SMO) infrastructures. Alternative absorber materials and etched/shifted multilayer stacks can provide long-term solutions for smaller features with smaller focus budget. Multi-objective optimization techniques can help to identify appropriate solutions.

Anamorphic imaging systems enable larger NA systems with manageable 3D mask effects. These systems help to reduce the contrast loss and the orientation dependency. In view of the small depth-of-focus (DoF) of larger NA systems, this has to be combined with mitigation strategies to avoid or compensate the mask-induced phase deformation and BF shifts.

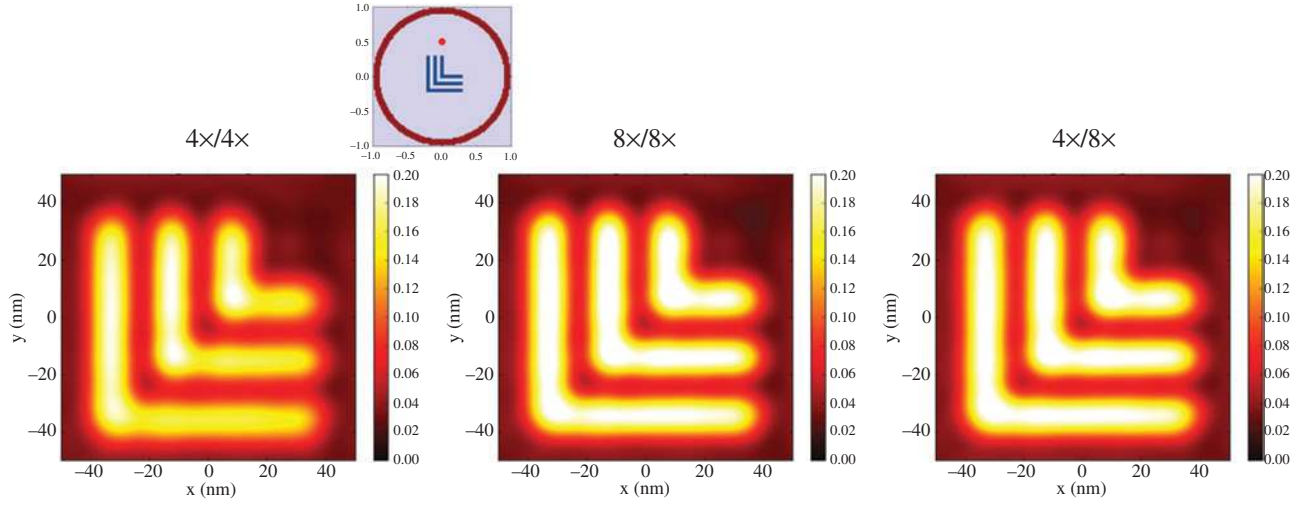

Figure 21: Simulated aerial images of elbow patterns consisting of 10-nm spaces. Annular illumination. All other parameters as given in Figure 20. The inset between the images of the 4×/4× and 8×/8× systems exhibits the orientation of the chief ray angle (red dot) with respect to the NA (circle) and the elbow layout on the mask.

Acknowledgments: This project has received funding from the Electronic Component Systems for European Leadership Undertaking under grant agreement number 662338. This Joint Undertaking receives support from the European Union's Horizon 2020 research and innovation program and the Netherlands, France, Belgium, Germany, Czech Republic, Austria, Hungary, Israel. The authors would like to thank Jens Timo Neumann and Paul Gräupner (Zeiss SMT) for their support and many technical discussions and Thorsten Last (ASML) for sharing figures on the source impact. All simulations were performed with the Fraunhofer IISB lithography simulator Dr.LiTHO.

References

[1] E. van Setten, G. Schiffelers, C. Toma, J. Finders, D. Oorschot, et al., Proc. SPIE 8886, 888604–888604–12 (2013).
[2] A. Wong and A. Neureuther, IEEE Trans. Semicond Manuf. 8, 419–431 (1995).
[3] A. Estroff, Y. Fan, A. Bourov and B. Smith, J. Micro/Nanolith. MEMS MOEMS 4, 031107–031107–8 (2005).
[4] D. Flagello, B. Geh, S. Hansen and M. Totzeck, J. Microlith. Microfab. Microsyst. 4, 031104 (2005).
[5] A. Erdmann and P. Evanschitzky, J. Micro/Nanolith. MEMS MOEMS 6, 031002 (2007).
[6] A. Erdmann, Proc. SPIE 4346, 345–355 (2001).
[7] J. Ruoff, J. Neumann, E. Smitt-Weaver, E. van Setten, N. le Masson, et al., Proc. SPIE 6730, 67301T (2007).
[8] J. Finders, Proc. SPIE 9052, 905205 (2014).
[9] J.-H. Ser, T.-H. Park, M.-G. Jeong, E.-M. Lee, S.-W. Lee, et al., Proc. SPIE 7640, 76401T (2010).
[10] J. Cheng, J. Schramm, D. Q. Zhang, Y. M. Foong, C. Zuniga, et al., Proc. SPIE 8326, 83261R (2012).
[11] A. M. Hawryluk, N. M. Ceglio, D. W. Phillion, D. P. Gaines, R. Browning, et al, Proc. SPIE 1547, 102–110 (1992).
[12] D. M. Tennant, L. A. Fetter, L. R. Harriott, A. A. MacDowell, P. P. Mulgrew, et al., Appl. Opt. 32, 7007–7011 (1993).
[13] K. B. Nguyen, A. K. K. Wong, A. R. Neureuther and D. T. Attwood, Jr., Proc. SPIE 1924, 418–434 (1993).
[14] B. Bollepalli, M. Khan and F. Cerrina, J. Vac. Sci. Technol. B 16, 3444–3448 (1998).
[15] T. V. Pistor, K. Adam and A. Neureuther, J. Vac. Sci. Technol. B 16, 3449 (1998).
[16] P. Schiavone, G. Granet and J. Robic, Microelectron. Eng. 57, 497–503 (2001).
[17] C. G. Krautschik, M. Ito, I. Nishiyama and K. Otaki, Proc. SPIE 4343, 392 (2001).
[18] P. Yan, Proc. SPIE 4562, 279 (2002).
[19] V. Philipsen, E. Hendrickx, E. Verduijn, S. Raghunathan, O. Wood, et al., Proc. SPIE 9235, 92350J (2014).
[20] C. Clifford and A. Neureuther, J. Micro./Nanolith. MEMS MOEMS 8, 031402 (2009).
[21] A. Erdmann, P. Evanschitzky, T. Bret and R. Jonckheere, Proc. SPIE 8679, 86790Y (2013).
[22] K. D. Badger, Z. J. Qi, E. Gallagher, K. Seki and G. McIntyre, J. Micro/Nanolith. MEMS MOEMS 12, 021004 (2013).
[23] M. Upadhyaya, V. Jindal, A. Basavalingappa, H. Herbol, J. Harris-Jones, et al., J. Micro/Nanolith. MEMS MOEMS. 14, 023505 (2015).
[24] V. Philipsen, E. Hendrickx, R. Jonckheere, N. Davydova, T. Fliervoet, et al., Proc. SPIE 8886, 88860B (2013).
[25] H. Kang, S. Hansen, J. van Schoot and K. van Ingen Schenau, Proc. SPIE 6921, 69213I (2008).
[26] C.-T. Shih, S.-S. Yu, Y.-C. Lu, C.-C. Chung, J. J. H. Chen, et al., Proc. SPIE 9422, 94220Y (2015).
[27] J. Finders, L. de Winter and T. Last, J. Micro/Nanolith. MEMS MOEMS 15, 021408 (2016).
[28] A. Erdmann, F. Shao, P. Evanschitzky and T. Fühner, J. Vac. Sci. Technol. B 28, C6J1 (2010).
[29] A. Erdmann, P. Evanschitzky, J. T. Neumann and P. Gräupner, J. Micro/Nanolith. MEMS MOEMS 15, 021205 (2016).
[30] T. Fühner, P. Evanschitzky and A. Erdmann, Proc. SPIE 8322, 83220I (2012).
[31] A. Szucs, J. Planchot, V. Farys, E. Yesilada, C. Alleaume, et al., Proc. SPIE 8683, 868313 (2013).
[32] M. K. Sears and B. Smith, J. Micro/Nanolith. MEMS MOEMS 12, 013008 (2013).
[33] V. Philipsen, K. V. Luong, E. Hendrickx, A. Erdmann, D. Xu, et al., Proc. SPIE 10147, 1014310 (2017).
[34] P. Y. Yan, Proc. SPIE 4889, 1099 (2002).
[35] Y. Deng, B. M. L. Fontaine, H. J. Levinson and A. R. Neureuther, Proc. SPIE 5037, 302 (2003).
[36] S.-I. Han, E. Weisbrod, Q. Xie, P. J. S. Mangat, S. D. Hector, et al., Proc. SPIE 5037, 314 (2003).
[37] M. Sugawara, A. Chiba and I. Nishiyama, Proc. SPIE 5037, 850 (2003).
[38] A. Erdmann, T. Fühner, P. Evanschitzky, J. Neumann, J. Ruoff, et al., Proc. SPIE 8679, 86791Q (2013).
[39] L. Van Look, V. Philipsen, E. Hendrickx, N. Davydova, F. Wittebrood, et al., Proc. SPIE 9661, 966109–966109–13 (2015).
[40] M. Burkhardt and A. Raghunathan, Proc. SPIE 9422, 94220X (2015).
[41] S. Hsu, R. Howell, J. Jia, H.-Y. Liu, K. Gronlund, et al., Proc. SPIE 9422, 94221I (2015).
[42] I. Mochi, V. Philipsen, E. Gallagher, E. Hendrickx, K. Lyakhova, et al., Proc. SPIE 9776, 97761S–97761S–17 (2016).
[43] Y.-G. Wang, A. Neureuther and P. Naulleau, in 'International Symposium on Extreme Ultraviolet Lithography' (Hiroshima, Japan, 2016).
[44] T. Last, L. de Winter, P. van Adrichem and J. Finders, J. Micro/Nanolith. MEMS MOEMS 15, 043508 (2016).
[45] L. Van Look, I. Mochi, V. Philipsen, E. Gallagher, E. Hendrickx, et al., in 'International Symposium on Extreme Ultraviolet Lithography' (Hiroshima, Japan, 2016).
[46] J. T. Neumann, P. Gräupner, W. Kaiser, R. Garreis and B. Geh, Proc. SPIE 8679, 867915 (2013).
[47] J. T. Neumann, M. Rösch, P. Gräupner, S. Migura, B. Kneer, et al., Proc. SPIE 9422, 94221H (2015).
[48] J. van Schoot, K. van Ingen Schenau, G. Bottiglieri, K. Troost, J. Zimmerman, et al., Proc. SPIE 9776, 97761I–97761I–15 (2016).
[49] S. Migura, B. Kneer, J. T. Neumann, W. Kaiser and J. van Schoot, Proc. SPIE 9661, 96610T (2015).
[50] M. P. Benk, A. Wojdyla, W. Chao, F. Salmassi, S. Oh, et al., J. Micro/Nanolith. MEMS MOEMS 15, 033501 (2016).